

Figure 4.11: (a) CV curves of different Co compounds in the Co redox region. (b) Calculation scheme of charge transfer during Co 2+/3+ and 3+/4+ redox reactions by integrating the redox peaks. (c) Charge transferred per surface area of tip and side surfaces of  $\text{LiCoO}_2$  during 2+/3+ and 3+/4+ redox processes.

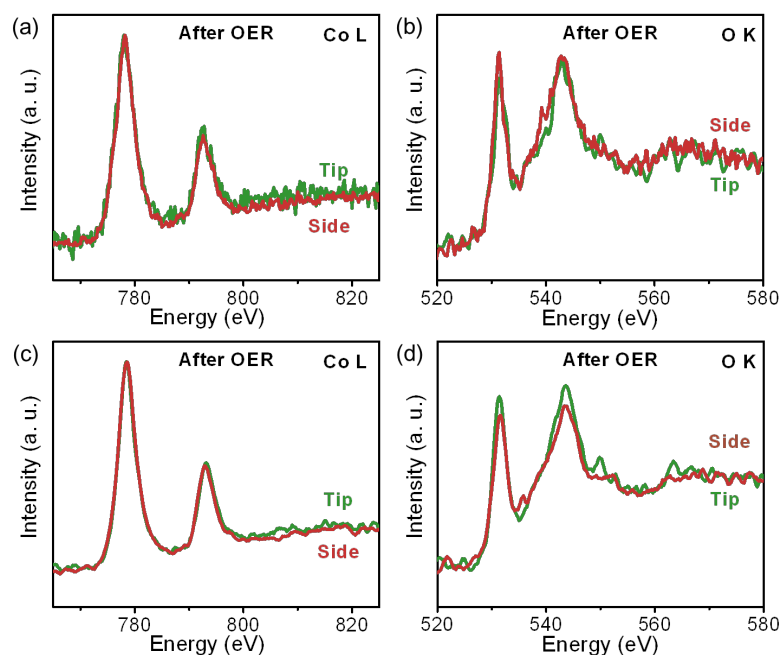


Figure 4.12. Two types of representative EELS spectra of 9 nm sample held at 1.55 V vs. RHE for OER. Upper row is one set of (a) Co L edge and (b) O K edge (case 1); bottom row (c) and (d) is the other set of spectra (case 2). These two types of spectra were observed at the same frequency on particles.

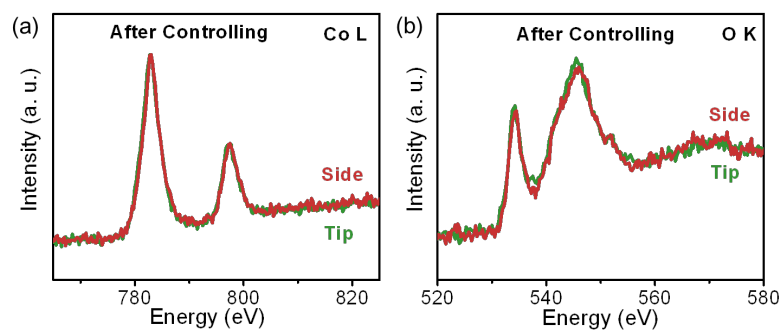


Figure 4.13. Representative EELS spectra of 9 nm sample that was immersed in 0.1 M KOH electrolyte for 1 hour without applying any potential. Then sample was rinsed by DI water and tried in air at room temperature. These spectra were taken under 300 kV. (a) Co L edge and (b) O K edge.

**Tables:**Table 4.1: Synthesis conditions and altered parameters to give the desired stoichiometric LiCoO<sub>2</sub> particle size.

LiCoO <sub>2</sub> Sample	Molten salt composition (molar ratio)	Heating time (hour)
10 nm	LiNO <sub>3</sub> -LiOH (6 : 4)	0.5
16 nm	LiNO <sub>3</sub> -KOH-LiOH (6 : 2.8: 1.2)	1
20 nm	KOH-LiOH (7 : 3)	0.5
30 nm	KOH-LiOH (7 : 3)	2
40 nm	KOH-LiOH (7 : 3)	6

Table 4.2: Rietveld Refinement fit parameters and the calculated  $a$  and  $c$  lattice parameters for the various sized stoichiometric  $\text{LiCoO}_2$  nanoparticles.

<b>Size (nm)</b>	<b><math>R_{wp}</math></b>	<b><math>R_b</math></b>	<b><math>a</math></b>	<b><math>c</math></b>	<b><math>c/a</math> ratio</b>
40	3.74	0.7717	2.816738	14.056028	4.990
30	4.27	0.7956	2.817727	14.065305	4.992
20	8.8	1.749	2.814981	14.062336	4.996
16	6.78	1.371	2.822156	14.069565	4.985
10	N/A				

Table 4.3: Calculated surface energy w/o spin transition compared with literature

Surface	Coordination # of oxygen	$\gamma$ (mJ/m <sup>2</sup> ) ref <sup>79</sup> with LS	$\gamma$ (mJ/m <sup>2</sup> ) this work with LS	$\gamma$ (mJ/m <sup>2</sup> ) this work spin trans.
{104}	5/6	1048	1118	312
{110}	4/6	2241	2227	1241

Table 4.4: The mass-normalized tip, side and total surface areas of each LiCoO<sub>2</sub> sample, computed using the particle size distributions collected from TEM images. The BET surface areas are also given for comparison. See detailed experimental session for more information.

	<b>9nm</b>	<b>14nm</b>	<b>31nm</b>	<b>40nm</b>
$S_{tip} \text{ (m}^2/\text{g)}$	8.9	7.8	4.4	3.3
$S_{side} \text{ (m}^2/\text{g)}$	133	111	40.4	26.7
$S_{total} \text{ (m}^2/\text{g)}$	142	118	44.8	30.0
$S_{BET} \text{ (m}^2/\text{g)}$	270	230	74	58

Table 4.5: The O K pre-peak area of tips and sides. The calculation method can be found in Figure S3. Samples were treated in O<sub>2</sub>-saturated electrolyte at 0.7 V, 1.55 V (vs. RHE) and without applying potential for 1 h for the post-OER, and post-ORR and controlling measurements, respectively. For each column, the pre-peak intensity of three different particles were calculated to give the average value and standard deviation in the table.

	9nm pristine	9nm controlling	9nm 0.7V		9nm 1.55V	
			Case 1	Case 2	Case 1	Case 2
Tip	3.21±0.11	4.05±0.29	2.84±0.44	4.38±0.31	3.49±0.14	4.44±0.23
Side	4.47±0.13	4.23±0.45	4.04±0.25	4.23±0.23	4.21±0.20	4.38±0.15

Table 4.6: The mass-normalized and total-surface normalized charge transfer during Co 2+/3+ and 3+/4+ redox processes of each LiCoO<sub>2</sub> sample, measured from CV current in 0.1 M KOH at 5 mV/s after the double-layer current correction (see Figure 4b). The charge transfer was integrated from 0.7 to 1.3 V vs. RHE for Co 2+/3+ redox and from 1.3 to 1.4 V vs. RHE for Co 3+/4+ redox, and was averaged between forward and backward scanning.

	<b>9nm</b>	<b>14nm</b>	<b>31nm</b>	<b>40nm</b>
$Q_{\text{Co}^{2+/3+}} \text{ (C/g)}$	240	198	74	56
$q_{\text{Co}^{2+/3+}} \text{ (C/m}^2\text{)}$	1.70	1.68	1.65	1.87
$Q_{\text{Co}^{3+/4+}} \text{ (C/g)}$	21	18	8	6.2
$q_{\text{Co}^{3+/4+}} \text{ (C/m}^2\text{)}$	0.14	0.15	0.18	0.21

Table 4.7: The Co L3/L2 ratios of tips and sides. The ratio was calculated after a double-step background correction.<sup>95</sup> Samples were treated in O<sub>2</sub>-saturated electrolyte at 0.7 V, 1.55 V (vs. RHE) and without applying potential for 1 h for the post-OER, and post-ORR and controlling measurements, respectively. For each column, the ratio of three different particles were calculated to give the average value and standard deviation in the table. The standard L3/L2 ratios for Co 2+, 3+ and 4+ are about 4.8, 2.8 and 2.0, respectively.<sup>95</sup>

	9nm pristine	9nm controlling	9nm 0.7V		9nm 1.55V	
			Case 1	Case 2	Case 1	Case 2
Tip	2.73±0.09	2.82±0.11	3.77±0.24	3.09±0.05	2.50±0.10	2.61±0.08
Side	2.70±0.11	2.80±0.12	3.07±0.15	2.92±0.05	2.74±0.15	2.63±0.09

## 5 UNCOVERING THE ROLES OF OXYGEN VACANCY ON CATION MIGRATION IN LITHIUM EXCESS LAYERED OXIDES

### 5.1 Introduction

In spite of researches on various kinds of materials in the past decades, lithium intercalation compounds still provide the best performances as the cathode materials for lithium ion batteries (LIB). Among all candidates, the lithium-excess layered oxides have gained growing research interests in recent years. It can reach more than 250 mAh/g capacity with average voltage of 4V, making it the candidate with highest energy densities among all known intercalation compounds for cathode materials.<sup>96-102</sup> Being source of major capacity improvement, the extra lithium ions, on the other hand, also cause unexplained phenomena in lithium-excess layered oxides. The rate performances of these materials are usually poor, and electron sources for the extra capacities have been under debate for years.<sup>99,103-106</sup> In classical layered oxides, the transition metal (TM) oxide host  $\text{TMO}_2$  should remain its host structure during initial discharging/charging, while lithium ions are intercalated/de-intercalated from the host. In contrast, recent studies suggested that in lithium-excess layered oxides, certain amount of surface transition metal ions migrate from the transition metal layers to lithium layers during the very first charging/discharging cycle.<sup>107-112</sup> These migrated ions are very stable in the lithium layers. They will likely block the lithium diffusion pathways and slow the lithium diffusion rates. Since the migrated surface transition metal ions could be one of the main factors that limit the material rate performances, and possibly cause instabilities in voltage profile, it is crucial to understand their diffusion mechanism. Our previous work<sup>29,30,112,113</sup> has suggested that the migration may be assisted by oxygen vacancies

generated in the late charging states of first cycle, but two critical questions remain unanswered: 1) how can we visualize the change in structure and chemical content at atomic level and 2) what is the energy required for oxygen vacancies formation upon cycling and how do they assist transition metal migrations. To answer these questions, a systematic study on generations of oxygen vacancies in Li-excess layered oxide  $\text{Li}[\text{Li}_{1/6}\text{Ni}_{1/6}\text{Co}_{1/6}\text{Mn}_{1/2}]\text{O}_2$  was performed using Scanning Transmission Electron Microscope / Electron Energy Loss Spectroscopy (STEM/EELS) experiments, and studies by first principles computational method were performed on its analogue  $\text{Li}[\text{Li}_{1/6}\text{Ni}_{1/4}\text{Mn}_{7/12}]\text{O}_2$ . EELS characterized the local oxygen and TM environments at the two phases and the interface region. The local diffusion barriers of TM ions were calculated with the presence of oxygen vacancy, and a hypothesis of transition metal ion migration mechanism is proposed.

## **5.2 Methodologies**

### **5.2.1 STEM/EELS**

Electron Microscopy work was carried out on a Cs-corrected FEI Titan 80/300-kV TEM/STEM microscope equipped with a Gatan Image Filter Quantum-865. All STEM images and EELS spectra were acquired at 300 kV and with a beam size of  $\sim 0.7\text{\AA}$ . EELS spectra shown in this work were acquired from a square area of  $\sim 0.5 \times 0.5$  nm with an acquisition time of 3 seconds and a collection angle of 35mrad. HAADF images were obtained with a convergence angle of 30mrad and a large inner collection angle of 65mrad. Images acquired by an HAADF detector with a small convergence angle and a relative large inner collection angle are also called “Z-contrast” images, where the

contrast is proportional to  $Z^{1.7}$ .<sup>114,115</sup> In atomic resolution Z-contrast images, the contrast of the atomic columns thus can be used to differentiate different elements and provide atomic-structural information.

To minimize possible electron beam irradiation effects, EELS and HAADF figures presented in this work were acquired from areas without pre-beam irradiation.

### 5.2.2. Computation details

First principles calculations were performed in the spin-polarized GGA+U approximations to the Density Functional Theory (DFT). Core electron states were represented by the projector augmented-wave method<sup>116</sup> as implemented in the Vienna ab initio simulation package (VASP).<sup>74,117,118</sup> The Perdew-Burke-Ernzerhof<sup>119</sup> exchange correlation and a plane wave representation for the wavefunction with a cutoff energy of 450eV were used. The Brillouin zone was sampled with a dense k-points mesh by Gamma packing. The four-layered supercell composed of 12 formula units of  $\text{Li}[\text{Ni}_{1/4}\text{Li}_{1/6}\text{Mn}_{7/12}]\text{O}_2$  used in previous work is used again to obtain the trend of oxygen vacancy formation energies. The atomic positions and cell parameters are fully relaxed to obtain total energy and optimized cell structure. To obtain the accurate electronic structures, a static self-consistent calculation is run, followed by a non-self-consistent calculation using the calculated charge densities from the first step. The cell volume is fixed with internal relaxation of the ions in the second step calculation. The Hubbard U correction was introduced to describe the effect of localized d electrons of transition metal ions. The applied effective U value given to Mn ions is 5eV and to Ni ions is 5.96eV.<sup>120</sup>

A new supercell composed of 24 formula units by doubling previous supercell along the c direction is used to investigate Ni diffusion mechanisms. Nudged Elastic Band (NEB) method is used to find the minimum energy path and the energy barrier for Ni diffusion inside the materials. All models are established as bulk materials, and no oxygen diffusion is considered in this work.

To calculate formation energies of oxygen vacancy in  $\text{Li}_x\text{Ni}_{1/4}\text{Mn}_{7/12}\text{O}_2$  bulk, both types of supercells were used for investigations and only one vacancy was created in each cell. This is equivalent to oxygen vacancy concentration between 2% to 4%, which satisfies the dilute defect conditions. Following two equations were used to calculate the formation energy of oxygen vacancies in  $\text{Li}_x\text{Ni}_{1/4}\text{Mn}_{7/12}\text{O}_2$ :

$$E_{fov} = E(\text{Li}_n\text{Ni}_3\text{Mn}_7\text{O}_{23}) + 1/2 E(\text{O}_2) - E(\text{Li}_n\text{Ni}_3\text{Mn}_7\text{O}_{24}) \quad (1)$$

and

$$E_{fov} = E(\text{Li}_m\text{Ni}_6\text{Mn}_{14}\text{O}_{47}) + 1/2 E(\text{O}_2) - E(\text{Li}_m\text{Ni}_6\text{Mn}_{14}\text{O}_{48}) \quad (2)$$

where  $E(\text{O}_2)$  is the calculated energy of the oxygen gas plus a 1.36 eV correction according to previous reports<sup>121</sup>.

### 5.3 Results and Discussions

To visualize the material structural change upon cycling from atomic level, aberration corrected high angle annular dark field (HAADF) STEM images of the material particles were obtained and shown in Figure 5.1(left). Similar to previous observations, TM ions were found in Li layer in the surface and subsurface region, forming a defect spinel structure that is different from the layered structure in bulk.<sup>112</sup> For

quantitative analysis, EELS experiments were carried out on the phase transformation region. Spatially resolved EELS were obtained at a step of  $\sim 0.6$  nm from surface to bulk and the spectra are presented in Figure 5.1(right). The data points are aligned with the STEM image to indicate where each spectrum was taken. For example, the black (data point 9) and red curves (data point 8) were acquired from the surface and near surface region, the blue (data point 7) curve was acquired from the spinel-layered interface, and the orange (data point 1) curve was acquired from the bulk. The onset energy of O K-edge pre-peak is aligned to 532eV. Therefore, our analysis of the O K-edge is limited to the fine structures and not the chemical shift of O K-edge. In Figure 5.1, there is a clear O pre-peak in the spectra obtained in bulk. This pre-peak starts to decrease when it comes to the interface region of the spinel-like and layer phase, and disappears completely in the spinel-like phase near surface. The splitting of the O K-edge usually corresponds to the splitting of the TM  $3d$  orbitals in six-coordinated environment. The disappearance of the pre-peak can be ascribed to the following two main reasons: 1) the neighbor TM being reduced; 2) oxygen vacancy formation, the splitting of neighbor TM  $3d$  orbitals is no longer the same as six-coordinated. Usually the TM reduction comes along with oxygen vacancy formation due to charge compensation. In this case, there were synchrotron XRD studies showing oxygen loss at the late charging state.<sup>122</sup> Therefore it is strongly evident that oxygen vacancies were presented mostly at the surface region where the spinel-like phase formed, and gradually disappeared when it came to the bulk of the layer phase.

From the STEM/EELS results, it is clear that TM ion migration only happens in the region where the oxygen vacancy presented. First principles calculations were then carried out for deeper understandings of the material from atomic level. As depicted in

the inset of Figure 5.2(a), each oxygen ion is bonded with 6 nearest cations. Three of them are Li ions in lithium layer and the other three in TM layer can be Li, Ni or Mn. There are four different combinations of the three cations in TM layer. These configurations are indicated by black circles in Figure 5.2(a) and noted by *a*, *b*, *c* and *d*. Oxygen vacancies can be located in these different local atomic configurations at different lithium concentrations. More than 70 calculations were performed with oxygen vacancies in different atomic configurations. A general trend of calculated oxygen vacancy formation energies ( $E_{fov}$ ) versus lithium concentrations is shown in Figure 5.2(b).

The lithium concentration of these calculations covers from 28/28 (fully lithiated) to 14/28 (half delithiated), the range of which correspond to the slopy region of the first charging voltage curve. It is clear that  $E_{fov}$  decreases sharply from  $\sim 2.7\text{eV}$  at fully lithiated state to less than  $1\text{eV}$  for Li concentration between 20/28 to 14/28. Note that at Li concentration 20/28, the tetrahedral Li-Li dumbbells begin to form, leading to the possible formation of spinel-like phases.<sup>112</sup> After that,  $E_{fov}$  becomes relatively stable. Our data show a surprisingly consistent trend of  $E_{fov}$  in terms of local atomic configurations.  $E_{fov}$  is usually low in configuration *d* while is usually high in configuration *a*. The results show a strong preference to certain local atomic environments for vacancy formation. Oxygen vacancies are more likely to form when their local environments are Li-Ni-Mn combinations in transition metal layer. Electrostatic effect may partially contribute to this phenomenon. As in the metal oxides, oxygen vacancies exhibit positive charges (Kroger notation  $\text{Vo}^{\bullet\bullet}$ ) therefore should be more stable near the cations with less positive charges.

In this work, all calculations were bulk calculations, while in reality, it is easier to form oxygen vacancies at material surfaces or sub-surfaces than in the bulk.

In order to investigate the migration mechanism of TM ions, the transition state theory is adopted in this work, as it has been extensively utilized to describe cation diffusion mechanism in the materials<sup>123</sup>. In  $\text{Li}_x\text{Ni}_{1/4}\text{Mn}_{7/12}\text{O}_2$ , both Ni and Mn ions are located originally in the octahedral site in TM layer. An empty tetrahedral site in Li layer is face-sharing with the TM octahedron. The shared-face is composed of three oxygen ions forming a triangular oxygen plane. When the three Li ions near the empty tetrahedral site are extracted, the TM ion may be able to migrate from the octahedral site to the empty tetrahedral site through the shared oxygen plane and then migrate to another octahedral site. If no oxygen vacancies present, the diffusion barriers for TM ions are usually high (0.7~0.8 eV for  $\text{Ni}^{2+}$ , 2.6 eV for  $\text{Mn}^{4+}$ , comparable to previous studies<sup>124</sup>), but the barriers can be significantly reduced when oxygen vacancies are introduced. The possible reasons of the large differences between  $\text{Ni}^{2+}$  and  $\text{Mn}^{4+}$  diffusion barriers are suspected to be their electronic structure differences as well as the higher charge of  $\text{Mn}^{4+}$ . Ni diffusions from initial octahedral sites in TM layer to the nearest tetrahedral sites in Li layer were investigated at three different Li concentrations:  $\text{Li}_{25/28}\text{Ni}_{1/4}\text{Mn}_{7/12}\text{O}_2$ ,  $\text{Li}_{20/28}\text{Ni}_{1/4}\text{Mn}_{7/12}\text{O}_2$  and  $\text{Li}_{15/28}\text{Ni}_{1/4}\text{Mn}_{7/12}\text{O}_2$  (shown in Figure 5.3). Three different Ni migration pathways are investigated when oxygen vacancies are introduced (shown in Figure 5.4): oxygen vacancy present 1) in the shared oxygen plane between octahedral site and tetrahedral site; 2) in the octahedral vertex but not in the shared oxygen plane; and 3) in the tetrahedral vertex but not in the shared oxygen plane. Although the exact values of Ni diffusion barriers are different for different diffusion paths, the trend is

consistent over all Li concentrations. Therefore only results at  $\text{Li}_{20/28}\text{Ni}_{1/4}\text{Mn}_{7/12}\text{O}_2$  are discussed below as the representative case. After the introduction of oxygen vacancy, the neighbor Ni will be reduced (Figure 5.5), therefore, the diffusion barrier of  $\text{Ni}^{2+}$  ions was investigated for a consistent comparison. Figure 5.4 shows the calculated Ni diffusion barriers at  $\text{Li}_{20/28}\text{Ni}_{1/4}\text{Mn}_{7/12}\text{O}_2$  with oxygen vacancies in different locations mentioned above. It is clear that the locations of oxygen vacancies have significant impact on the Ni diffusion barriers. When Ni diffuses through the shared oxygen plane with vacancy, although the oxygen electron charge density may be less dense, the Ni diffusion barriers are around 1eV, which are slightly higher than the barriers without oxygen vacancies. When Ni migrates from five-coordinated octahedral site, it will be much more unstable in the regular tetrahedral site and Ni diffusion barriers are reduced to as low as 0.2 eV to 0.5 eV. When the vacancy appears at the tetrahedral vertex, which is not in the shared oxygen plane, the three-coordinated tetrahedral site becomes unstable with significant valence change of nearby transition metal ions. In this case, calculated Ni diffusion barrier is a mixing of barriers raised from Ni ion migration and charge transferring between ions, therefore is not included in Figure 5.4. A study on Mn diffusion was also performed at  $\text{Li}_{20/28}\text{Ni}_{1/4}\text{Mn}_{7/12}\text{O}_2$ , and similar observations were obtained (shown in Figure 5.6). With no oxygen vacancies, Mn is much more stable in the octahedral site than in the tetrahedral site, and the barrier is as high as 2.6 eV. However, when oxygen vacancy is introduced in octahedral site but not in the shared plane, the diffusion barrier can be reduced to  $\sim 0.7$  eV. Besides, if oxygen vacancy is introduced in tetrahedral site but not the shared plane, Mn becomes very unstable in the three-coordinated tetrahedral site and will automatically diffuse to nearby octahedral site with no barrier. How oxygen vacancy

would assist TM migration is shown quantitatively for the first time from computations; our findings reveal that during the oxygen vacancy presence both Ni and Mn have the potential to diffuse at room temperature and Ni has lower barrier, while the experimental evidence needs future investigations.

#### **5.4 Conclusions**

Combining both STEM/EELS experimental observations and first principles computational studies, we demonstrated that in the Li-excess materials oxygen vacancies are presented in these regions and assisting the TM ion migration through a novel mechanism proposed below: during first cycle charging, after most TM ions are fully oxidized, oxygen ions start to participate in oxidation process (lose electron) and oxygen vacancies would form with formation energy about 0.5-0.6eV. Possibly due to the slow oxygen migration, oxygen vacancies mostly form near the material surfaces and sub-surfaces with 5-6 atomic layers. A significant fraction of the TM ions in these regions therefore are subjected to five (or even less) O-coordinated due to either presences of oxygen vacancies or the broken TM-O bonds on the particle surfaces. TM ions in those five (or less) O-coordinated defect polyhedral sites become much unstable and will spontaneously migrate to the fully-coordinated polyhedral sites nearby in the Li layer. On the other hand, although many of the Li ions are extracted upon charging, stable Li-Li dumbbells are also formed leaving only certain sites in Li layers that are available for TM occupation. Combination of the above two reactions therefore causes the formation of a spinel-like phase from material surface towards the bulk until reaching a region (2~3 nm

beneath surface after first cycle) where oxygen vacancy concentrations are too low to assist the TM ion migration. It was reported that although it might be subjected to further phase change, this TM-ion-migrated region is present for 50 cycles with its thickness unchanged.<sup>32</sup> Our work rationalizes these observations and shed light on the atomic level structure change upon cycling in this class of high energy density cathode materials. The critical role of oxygen ions must be considered for further optimization of this class of materials. Surface coating or doping elements with stronger affinity to oxygen is expected to reduce the phase transformation.

Chapter 5, in full, is a reprint of the material “Uncovering the roles of oxygen vacancies in cation migration in lithium excess layered oxides”, *Phys. Chem. Chem. Phys.*, 2014, 16, 14665. The dissertation author was the primary investigator and author of the paper.

Figures:

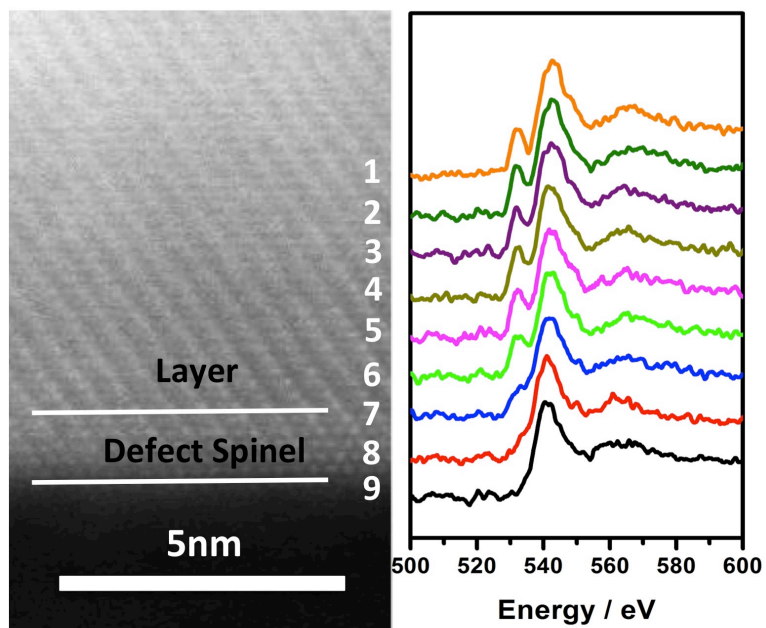


Figure 5.1: Spatial resolved O K-edge EELS spectra from bulk to surface.

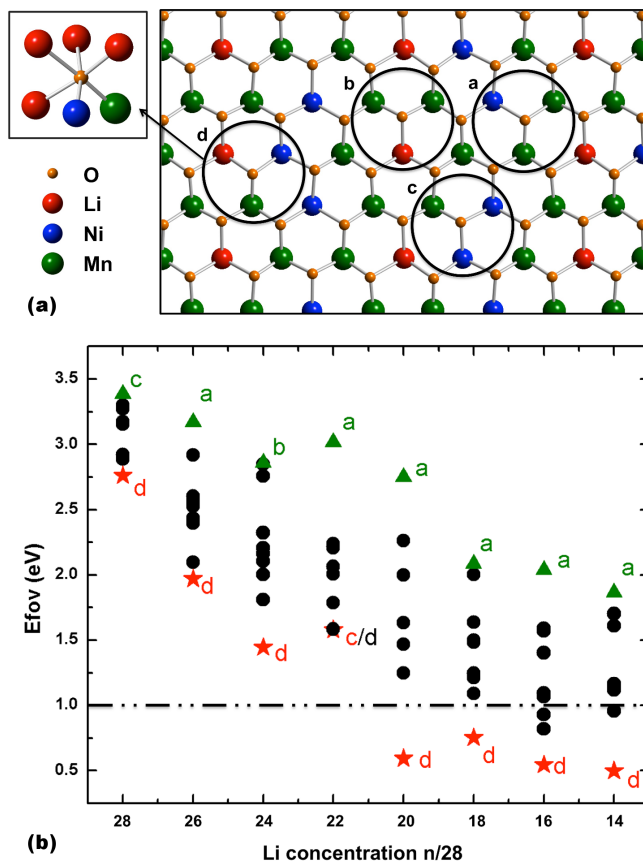


Figure 5.2: (a) Atomic configurations of  $\text{Li}[\text{Li}_{1/6}\text{Ni}_{1/4}\text{Mn}_{7/12}]\text{O}_2$ ; (b) Oxygen vacancy formation energy vs. Li concentration

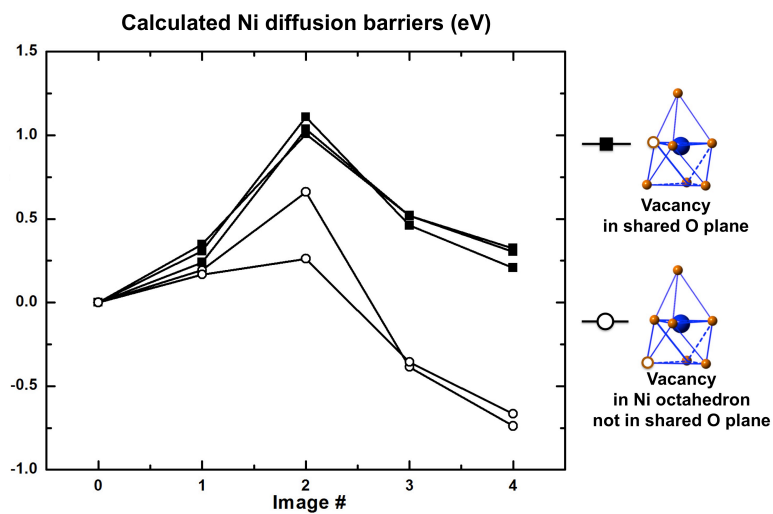


Figure 5.3: Ni diffusion barriers with oxygen vacancies in different positions at  $\text{Li}_{15/28}\text{Ni}_{1/4}\text{Mn}_{7/12}\text{O}_2$

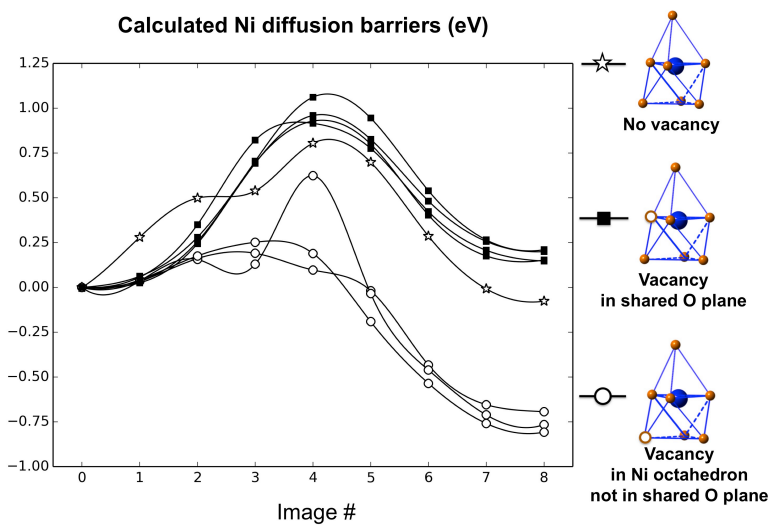


Figure 5.4: Calculated Ni diffusion barriers with oxygen vacancies in different positions at  $\text{Li}_{20/28}\text{Ni}_{1/4}\text{Mn}_{7/12}\text{O}_2$  (Vacancy in tetrahedron but not in the shared plane unstable)

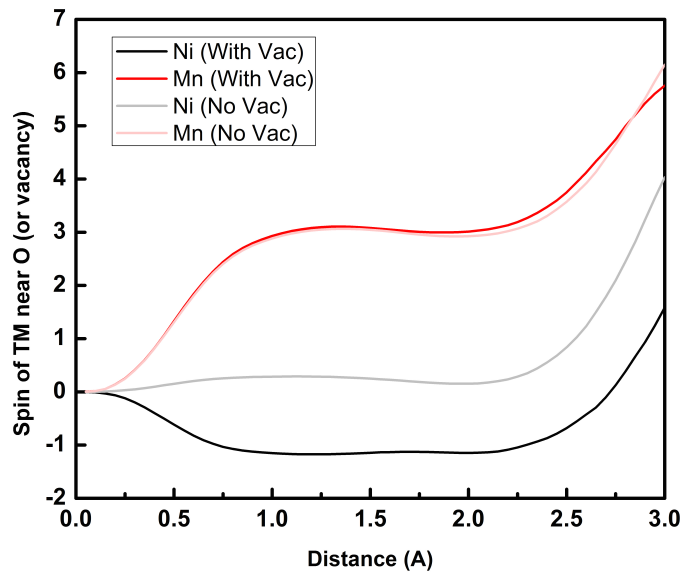


Figure 5.5: Neighboring TM valence change after introduction of oxygen vacancy at  $\text{Li}_{20/28}\text{Ni}_{1/4}\text{Mn}_{7/12}\text{O}_2$

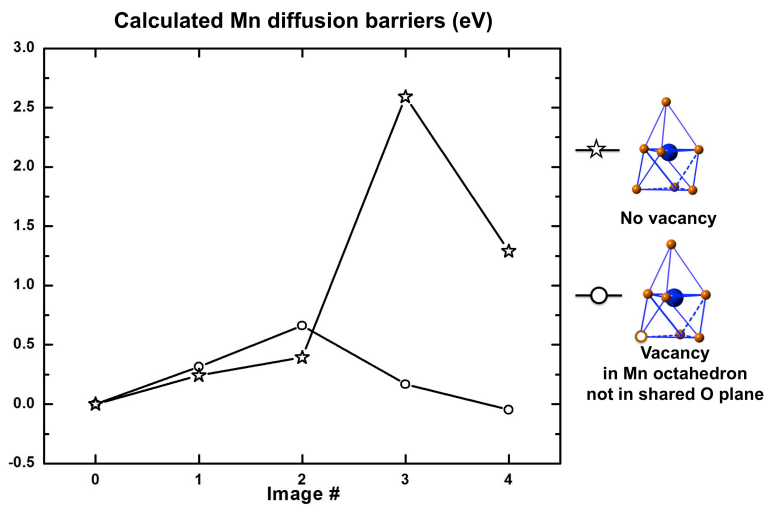


Figure 5.6: Mn diffusion barriers with oxygen vacancies in different positions at  $\text{Li}_{20/28}\text{Ni}_{1/4}\text{Mn}_{7/12}\text{O}_2$

## 6 SURFACE COATING ON CATHODE MATERIALS IN LIB

### 6.1 Lithium lanthanum titanium oxides: a fast ionic conductive coating for lithium-ion battery cathodes

#### 6.1.1 Introduction

Lithium Lanthanum Titanate (LLTO) is one of the fastest lithium ion conductors to date.  $\text{Li}_{3x}\text{La}_{(2/3)-x}\text{Ti}_{(1/3)-2x}\text{TiO}_3$  adopts the perovskite structure  $\text{ABO}_3$  with  $\text{A}=\text{Li}$ ,  $\text{La}$  and  $\text{B}=\text{Ti}$ .<sup>125-130</sup> This series of materials are considered to have fast lithium transportation and the bulk ionic conductivity can be achieved as high as  $1 \times 10^{-3} \text{ Scm}^{-1}$  at room temperature when  $x=0.11$ .<sup>131,132</sup> Applying this material as the solid electrolyte in all-solid Li-ion battery is under intensive studies.<sup>133-135</sup>

At present, the electrolyte of secondary lithium ion batteries in the market is mainly based on  $\text{LiPF}_6$  salt dissolved in an organic solvent (such as ethylene carbonate). Electrolyte needs to be a fast Li ion conductor, but an electron insulator. A major concern about the liquid electrolyte is the safety issue, including poor thermal stability and low resistance to leakage. In addition, conventional electrolyte has narrow voltage window, decomposition would happen at both extremely low and high voltage ranges causing electrode/electrolyte parasitic reactions. Upon cycling, the electrolyte would get consumed and the cell eventually fails. Solid electrolyte can mitigate these problems but to have fabricate a continuous layer of solid electrolyte layer at large dimensions remains a major challenges. In this study, we are applying solid electrolyte as a coating material for cathode in lithium ion batteries to resolve the current issues in the second-generation layered transition metal oxide materials, such as  $\text{LiNi}_{0.8}\text{Co}_{0.15}\text{Al}_{0.05}\text{O}_2$  (NCA).

The current problems (fading capacity and poor cyclability etc.) present in pristine NCA layered cathode material have been attributed to the dissolution of the cation into the electrolyte, as well as the surface layer-to-spinel phase transformation happening in most layered materials.<sup>112</sup> Coatings such as  $\text{AlF}_3$ ,  $\text{ZrO}_2$ ,  $\text{Al}_2\text{O}_3$  etc. have been studied intensively to improve the performance. Suppression of the phase transitions, increases in the structural stabilities, as well as decreases in the disorder of cations in the crystal sites have been observed. However the surface modification mechanism still remains open for different coating materials. Furthermore, few studies have been reported on the characterization of continuous effect of coating upon cycling.

In this study, first principles calculations were performed to explore the lithium diffusion pathways and calculate the lithium diffusion activation barriers in  $\text{Li}_{3x}\text{La}_{(2/3)-x}\text{TiO}_3$  when  $3x = 0.125$  and  $0.35$ . To study the effect of LLTO as a coating for cathodes, the LLTO coating has been applied to  $\text{LiNi}_{0.8}\text{Co}_{0.15}\text{Al}_{0.05}\text{O}_2$  (NCA). We show significantly improved electrochemical performances of the coated samples. To systematically study the mechanism of a solid electrolyte as a coating material to cathode, scanning electron microscope (SEM), energy dispersive spectroscopy (EDS), X-ray diffraction (XRD), transmission electron microscope (TEM) combined with electrochemical property measurements including PITT and EIS were carried out on both the pristine NCA sample and LLTO coated sample. Scanning transmission electron microscope with electron energy loss spectroscopy (STEM\_EELS) mapping was collected on coated sample before and after cycling.

## 6.1.2 Methodologies

### 6.1.2.1 Computational Methodology

In this work, two models of  $\text{Li}_{3x}\text{La}_{(2/3)-x}\text{TiO}_3$  are created with low lithium concentration ( $x=1/24$ ) and high lithium concentration ( $x=7/60$ ). For low-lithium-concentration LLTO, the atomic models and notations are adopted from previous work done by Catti.<sup>136,137</sup> The supercell is composed of eight formula units of  $\text{Li}_{0.125}\text{La}_{0.625}\text{TiO}_3$ . For high lithium concentration LLTO, an original model is proposed in this study with twenty formula units of  $\text{Li}_{0.35}\text{La}_{0.55}\text{TiO}_3$ . First principles calculations were performed in the spin-polarized GGA+U approximation to the Density Functional Theory (DFT). Core electron states were represented by the projector augmented-wave method<sup>73</sup> as implemented in the Vienna ab initio simulation package (VASP).<sup>74,75</sup> The Perdew Burke Ernzerhof correlation<sup>74</sup> and a plane wave representation for the wavefunction with a cutoff energy of 420eV were used. The Brillouin zone was sampled with a mesh including gamma point. The density of the k-point mesh for all calculations is approximately one point per  $0.01 \text{ \AA}^{-3}$ . The atomic positions and cell parameters were fully relaxed to obtain total energy and optimized cell structure. Effective U value is applied in the Liechtenstein approach with exchange energy  $J = 1.0\text{eV}$ .<sup>76,138</sup>  $U_{\text{eff}} = 7.5\text{eV}$  is applied to the La 4f states to correct their position relative to La 5d levels.<sup>139</sup> It is reported that the experimentally observed position of 4f bands can be reproduced within this approach.<sup>140</sup> The Nudged Elastic Band (NEB) method is used to find the minimum energy path and the energy barrier for Li diffusion in LLTO.<sup>141</sup>

### 6.1.2.2 Experimental Methodology

*Materials:* All the samples, NCA pristine sample with particle size of around 100nm, together with 1wt%, 2wt% and 5wt% LLTO coated NCA samples (named as LLT1, LLT2 and LLT5, respectively), are synthesized by the company CheMat Technology.

*Materials Characterization:* The particle morphology and size distribution of the synthesized powders were determined using an FEI XL30UHR SEM (ultra high resolution SEM) with a Sirion column, which enables very high resolution imaging at low kV. All images were collected under an accelerating voltage of 10kV. The powders were suspended on a double-sided carbon tape placed on a specimen holder.

EDS was taken using a Phillips XL30 field-emission environmental high resolution SEM with an Oxford EDS attachment.

XRD spectra were taken using a Bruker D8 advance diffractometer with a Bragg Brentano theta-2theta geometry and a Cu K $\alpha$  source. Samples were scanned from 10° to 80° with a scan rate of 0.025° per second.

TEM images were collected using an FEI Tecnai G2 Sphera cryo-electron microscope with an operation voltage of 200kV. The powders were suspended on a 300mesh copper grid with lacey carbon.

STEM-EELS data was collected using a Cs-corrected FEI Titan 80/300-kV TEM/STEM microscope equipped with a Gatan Image Filter Quantum-865. All STEM images were acquired at 300kV. EELS spectra shown in this work were acquired with a convergence angle of 30mrad.

### 6.1.2.3 Electrochemical Characterization

Cathodes were prepared by mixing 80 wt % pristine and coating powder with 10 wt % acetylene carbon black (99.9%) and 10 wt % poly (vinylidene fluoride) in *N*-methyl pyrrolidone solution. The slurry was cast onto Al foil using a doctor blade and dried overnight in a vacuum oven at 80°C. The electrode disks were punched and dried again at 80°C for 6h before storing them in an argon- filled glove box ( $\text{H}_2\text{O}$  level of  $<1$  ppm). 2016 type coin cells were used to study the electrochemical behavior of the compounds. Lithium metal ribbon and 1 M  $\text{LiPF}_6$  in a 1:1 EC: DMC solutions were used as anode and electrolyte, respectively. A Celgard model C480 separator (Celgard Inc.) was used as the separator. The coin cells were assembled in the same argon-filled glove box and tested on an Arbin battery cycler in galvanostatic mode. The cycling tests were conducted between 2.5V and 4.2V and the rate tests were in the window of 2.0V-4.4V.

The PITT experiments were carried out by applying potential steps of 10 mV and measuring the current as a function of time for the first charge. The potential step was advanced to the next level when the measured current fell below the threshold limit of 10  $\mu\text{A}$ , corresponding to a  $C/200$  rate. The voltage window was set at 3.45-4.2 V.

Solartron 1287 system coupled with a Solartron 1260 frequency response analyzer was used for the EIS measurement. The EIS test was carried out using the three-electrode cell. For the reference electrode, the end tip of the Teflon-coated Cu wire ( $\phi(\text{Teflon})=4.5\times 10^{-4}$  m;  $\phi(\text{Cu})=1.27\times 10^{-4}$  m) was removed and placed between two separators. Details on cell configuration can be found elsewhere.<sup>142,143</sup> Before the electrochemical experiments, elemental Li was cathodically coated on the bare Cu wire by having Li metal as a counter

electrode. The as-prepared cell was charged to and equilibrated at 4.2 V at a rate of C/10. The impedance spectra were obtained in the frequency range of 100 kHz to 100 mHz.

### 6.1.3 Results

#### 6.1.3.1 Computational Results

##### 6.1.3.1.1 Low lithium concentration scenario

The atomic structure of  $\text{Li}_{0.125}\text{La}_{0.625}\text{TiO}_3$  is shown in Figure 6.1(a). For low-lithium-concentration LLTO, the atomic models and notations are adopted from previous work done by Catti et. al.<sup>136,137</sup> The supercell is composed of  $2a_p \times 2a_p \times 2a_p$ , where  $a_p$  is the conventional cubic lattice of  $\text{ABO}_3$  perovskite structure (38 atoms in total). La ions are located in A sites and Ti ions in B sites. Li ions are also located in A sites as initialization. Along (001) direction, four A-site ions in (001) plane can be grouped as a 2D cell. A La-rich layer ( $z=1/4$ ) is composed of 4 La ions (4La) and a La-poor layer ( $z=3/4$ ) composed of 1 La ion, 1 Li ion and 2 vacancies (1La+1Li+2 $\square$ ) (shown in Figure 6.1(b)). This La-rich and La-poor layers are alternatively arranged according to the experimental observations.<sup>144</sup> The after relaxation structure of  $z=3/4$  plane is shown in Figure 6.1(c). After structural relaxation, the cubic lattice is distorted to an orthorhombic lattice where  $a=7.828\text{\AA}$ ,  $b=7.754\text{\AA}$ ,  $c=7.871\text{\AA}$ . La and Ti ions are still in A and B sites respectively, while Li ions move closely to the center vertical oxygen square planar window as shown in Figure 6.2(b) and (c). These results are consistent with the previous work.<sup>137</sup> These sites are referred as Li equilibrium sites in this work. Figure 6.2(a) shows all the Li equilibrium sites in the 2D La-poor layer. These equilibrium sites are used as